Dual-plane stereoscopic PIV measurement of vortical structure in turbulent channel flow on sinusoidal riblet surface

H. Mamori[a], K. Yamaguchi[b], M. Sasamori[c], K. Iwamoto[b,*], A. Murata[b]

[a] *Department of Mechanical and Intelligent Systems Engineering, The University of Electro-Communications, 1-5-1, Chofugaoka, Chofu, Tokyo 182-8585, Japan*
[b] *Department of Mechanical Systems Engineering, Tokyo University of Agriculture and Technology, 2-14-26 Nakacho, Koganei, Tokyo 184-8588, Japan*
[c] *Japan Aerospace Exploration Agency*

Abstract

Vortical structure in wall turbulence over a sinusoidal riblet surface is investigated by means of a dual-plane stereoscopic particle image velocimetry (DPS-PIV) measurement. The experiment is made in a channel flow at a friction Reynolds number of 150. The lateral spacing of the adjacent walls of the sinusoidal riblet varies in the streamwise direction and 12% of the drag reduction rate has been confirmed. The DPS-PIV measurement system consists of four high-speed CCD cameras. The laser sheets are provided on streamwise and wall-normal planes and separated 0.5 mm in the spanwise direction to each other. The profiles of the velocity statistics in the flat case show a good agreement with previous data. Since all velocity components can be measured on adjacent laser sheets simultaneously, an instantaneous velocity deformation tensor can be obtained and vortical structures can be identified by a second invariant of the tensor i.e., the Q value. The probability of Q value in the riblet side is almost unchanged from that of the flat side. The analysis of the tracking of vortical structures by using the Q value is performed. As similar to a pathline analysis in a previous study, we confirmed that the riblet surface prevents the vortical structure hitting the wall and vortical structures follow the upward and

*Corresponding author
Email address: iwamotok@cc.tuat.ac.jp (K. Iwamoto)

downward flows induced by the sinusoidal riblet surface.

Keywords: turbulent flow, drag reduction, sinusoidal riblet, dual-plane PIV measurement

2016 MSC: 00-01, 99-00

1. Introduction

Skin friction drag in turbulent flows significantly increases owing to activity of vortical structures near walls. However, it is known that skin friction drag decreases due to riblet surfaces, which are grooves aligned in the streamwise direction on wall surfaces. Up to now, numerous types of two-dimensional riblet surfaces have been investigated experimentally and numerically (e.g., Walsh [1, 2, 3]; Bechert *et al.* [4]; Choi *et al.* [5]; El-Samni *et al.* [6]; Garcia-Mayoral and Jimenez [7]; Boomsma [8]).

Walsh [1] made experimental studies for the turbulent boundary layer flow over the v-grooved 2D riblet surface and confirmed the drag reduction effect of 8% at the momentum thickness Reynolds number of 867 to 3900 (the corresponding friction Reynolds number is 4300 to 44000). Bechert *et al.* [4] optimized the riblet shape and found 10% of the maximum drag reduction rate on thin blade riblets at $\mathrm{Re}_\tau = 500 \sim 10400$. They considered two-dimensional (2-D) riblets, whose lateral spacings are kept constant in the streamwise direction. Choi *et al.* [5] performed direct numerical simulations (DNS) of turbulent channel flows with the v-groove riblet surface and confirmed the drag reduction rate of 5-6% when the lateral spacing of the riblet walls is 20 in the wall unit. Difference in statistics between the riblet and flat cases was found in the region near the walls and the quadrant analysis showed the decrease of the drag increasing events (i.e., sweep and ejection events). They suggested the drag reduction mechanism of the riblet surface related to vortical structure: since the lateral spacing of the riblet is narrower than the diameter of the quasi-streamwise vortex (referred as QSV), QSVs are kept away from the wall and the downwash motion of the vortices is suppressed, resulting in the drag

reduction. This effect has also been confirmed in thin rectangular riblets by El-Samni *et al.* [6] and in semi-circular grooves by Lee and Lee [9]. Suzuki and Kasagi [10] performed particle tracking measurement (PTV) over a v-groove riblet surface at the bulk Reynolds number of 5100 and 12000 ($\mathrm{Re}_\tau = 335$ and 710) and proposed another drag reduction mechanism of riblets: attenuation of the splatting phenomenon causes a decrease of QSV regeneration. It is reported that the maximum drag reduction by the riblet surface decreases as increasing the Reynolds number [11, 12, 13].

The virtual origin of the wall-normal coordinate and the definition of the "channel half-width" are important concept for the riblet surface. If the riblet width is small (i.e., the viscous regime), the drag reduction effect can be predicted by using the concept of the virtual origin or the protrusion height. Bechert and Bartenwerfer [14] investigated the viscous sublayer of the flow on a riblet surface theoretically by using a conformal mapping and determined "virtual origin" of a longitudinal flow. The virtual origin is the location of an *imaginary flat surface* and lies somewhat below the tip of the riblet [5]. Bechert and Bartenwerfer [14] defined the protrusion height as the distance between the origin and the tip of the riblet and suggested that the drag reduction occurs if the protrusion height is small. Luchini *et al.* [15] defined the virtual origin of the cross flow and noted the importance of the protrusion height which is defined as difference between the virtual origin for longitudinal and cross flows. If the virtual origin for the cross-flow is higher than that for the longitudinal flow, the streamwise vortical structures are impeded and displaced away from the wall. The streamwise vortical structure is attenuated, which results in the skin-friction drag reduction. By using the concept of the protrusion height, Bechert *et al.* [4] derived an equation for the drag reduction rate R_D as

$$R_D = \frac{0.785\,(\Delta h/s)\,s^+}{(2c_f)^{-1/2} + 1.25}, \tag{1}$$

where Δh is the protrusion height, s is the riblet width, c_f is the skin-friction coefficient. Equation (1) shows that the drag reduction rate depends on the protrusion height and increases linearly with increasing the riblet width.

Inspired by two-dimensional riblets, three-dimensional riblets have been developed since these have the possibility to provide a higher drag reduction effect than that of the optimized 2-D riblet. The "three dimensional riblet" means that a riblet shape varies in the streamwise direction. Bechert *et al.* [16] made the experimental study of the three-dimensional riblet at the channel Reynolds number of 10000 to 30000. Their riblet was an idealized model of shark skin and they confirmed 7.3% of the drag reduction. Another three-dimensional riblet was the wavy riblet [17, 18] aiming to obtain an effect similar to the spanwise oscillation technique. Okabayashi [19] modified the sinusoidal wavy wall riblet (see also, Okabayashi [20]). In addition, Benschop and Breugem [21] confirmed the drag reduction effect by the herringbone riblet texture.

Sasamori *et al.* [22] evaluated one of the three-dimensional riblets, i.e., a sinusoidal riblet surface which provides up to 11.7% of the drag reduction rate in a turbulent channel flow at $\mathrm{Re}_\tau = 150$. In the sinusoidal riblet surface, it is difficult to predict the drag reduction rate by using Eq. (1) because the lateral spacing of the riblet walls varies in the streamwise direction. They concluded that the drag reduction mechanism of the sinusoidal riblet is similar to that of the 2-D riblet while the average of the lateral spacing of the sinusoidal riblet surface is larger than the diameter of the vortices. A two-dimensional PIV measurement on the streamwise and wall-normal plane over the sinusoidal riblet surface shows decreases of the root-mean square values of velocity fluctuation and Reynolds shear stress. Sasamori *et al.* [22] performed a pathline analysis and revealed that the riblet prevents "vortex approaching" toward the wall, owing to the induced upward and downward flows (This effect is confirmed by means of the DNS [23]). In consequence, the wetted area of the sinusoidal riblet is smaller than those of 2-D riblets, resulting in the high drag-reduction effect. Their pathline analysis, however, did not track the vortical structure directly. In the present study, we employ the DPS-PIV measurement system to clarify the influence of the sinusoidal riblet on the vortical structure.

QSVs are well known to sustain high skin friction drag in wall turbulence. The Q criterion, the second invariant of the velocity deformation tensor, is of-

ten employed to identify vortical structures (Hunt *et al.* [24]); however, it is difficult to evaluate the Q criterion experimentally due to the limitation on velocity measurements: the Q criterion requires all nine velocity gradients. Therefore, the investigation has been restricted to numerical simulations (e.g., Kasagi *et al.* [25]; Tanahashi *et al.* [26]).

Particle image velocimetry (PIV) has been widely used to reveal flow behavior experimentally. It has an advantage of capturing the spatial distribution of velocity field simultaneously with contactless measurement. Recently, thanks to the development of PIV measurement techniques, it has been possible to obtain all velocity gradients without applying any assumptions. The dual-plane stereoscopic PIV system (referred as DPS-PIV, hereafter) is a simple PIV-based technique to obtain all velocity derivatives. It consists of two sets of stereoscopic PIVs and two differentially spaced laser sheets. Kähler and Kompenhan [27] first introduced DPS-PIV measurements. Note that they called it the multiple plane stereo PIV. They applied two orthogonally polarized laser sheets and beam splitters so that one stereoscopic camera could film scattering images on only one laser sheet. Hu *et al.* [28] used the same system on a lobed jet flow and evaluated the accuracy of the DPS-PIV measurement. Unlike their techniques, which use orthogonally polarized light sheets and beam splitters, Mullin and Dahm [29, 30, 31] applied two different frequency laser sheets and narrow-band filters separating scattered light appropriately. Tanahashi *et al.* [32] developed time-resolved DPS-PIV including optical system which requires only two single-pulse Nd:YAG lasers while the earlier mentioned DPS-PIV systems needs four lasers. Furthermore, they evaluated QSVs on a turbulent jet flow and revealed that the diameter and maximum azimuthal velocity of QSV were consistent with those analyzed by direct numerical simulation.

In the present study, we focus on the vortical structures over the sinusoidal riblet surface in order to reveal the relationship between the drag reduction effect and the turbulent structures in detail. The vortical structures are identified according to the Q criterion by means of a DPS-PIV measurement. The DPS-PIV can provide all the velocity components and deformation tensors. The objec-

tive of the present study is to obtain the statistics of the velocities around the vortical structures and reveal vortex behavior over the riblet surface. Our previous studies performed the two-dimensional PIV measurement for wall-normal plane [22] and the DNS study of turbulent channel flows [23]. The contribution of the present paper, in contrast, is to measure the Q value directly by the DPS-PIV measurement and analyze the behavior of vortical structure.

2. Experimental set-up

The DPS-PIV measurement is performed in a rectangular duct flow. The skin friction Reynolds number is set to be $\mathrm{Re}_\tau = 150$ which is defined by the half height of the duct δ, the kinematic viscosity ν and the friction velocity u_τ on the smooth surface. The friction velocity u_τ on the smooth surface is estimated from the stream velocity profile obtained by PIV measurement. The calculation method for u_τ is mentioned in 2.1.

The wind tunnel consists of a developing section and a test section: the former is 3m long and the latter is 4m long. The cross-sectional dimensions of the wind tunnel are $200 \times 20\mathrm{mm}^2$. The duct half height δ= 10 mm is measured by a laser displacement sensor at 332.5δ downstream from the entrance of the test section. The working fluid is air. The base flow is driven by a blower at the downstream end of the wind tunnel. The mass flow rate is adjusted by the rotating speed of the blower. We install the turbulence grid at the inlet of the entrance section to provide a fully developed turbulent flow at the inlet of the test section. As shown later, we have confirmed that the measured flow statistics well agree with those in the fully developed channel flow obtained by the DNS. The sinusoidal riblet is installed on the bottom wall of the test section. The upper wall is the flat surface.

Figure 1 shows the geometry of the sinusoidal riblet surface. The sinusoidal riblet is made from acrylonitrile butadiene styrene (ABS) resin and milled by a computer numerical control machining center. The wavelength of the sinusoidal riblet is 360 in the wall unit and the lateral spacing of it varies in the streamwise

direction sinusoidally. An averaged lateral space is 36 in the wall unit, which is larger than that of the 2-D riblet (e.g., Choi *et al.* [5]). Thus, a number of the walls of the sinusoidal riblet decreases for the unit area and the wetted area of the sinusoidal riblet is smaller than that of the 2-D riblet. The design parameters are determined based on the parametric study by the DNS (Sasamori *et al.* [23]) and its drag reduction effect is confirmed by the experiment (Sasamori *et al.* [22]). The superscript of plus indicates the wall unit: variable is nondimensionalized by u_τ of the flat side and ν.

2.1. DPS-PIV measurement

The DPS-PIV measurement is conducted at 3.7 m downstream from an entrance of the test section where the fully developed flow has been confirmed. The DPS-PIV measurement consists of two individual stereoscopic PIV systems and two laser light sheets. The laser beams with 532 nm wavelength are generated by two Nd:YAG lasers and rotated 45 degrees by a half-wave plate. The laser beams thereby contain both horizontal and vertical polarizations and each polarized beam is separated by using beam splitters and mirrors. The two laser beams are then expanded by a cylindrical lens and illuminate two streamwise and wall-normal planes. Note that the optical system for generating two parallel laser sheets is the same as that used by Tanahashi *et al.* [32]. In order to separate the scattered light onto the other plane, the two lasers are polarized in both the vertical and horizontal directions and separated by beam splitters installed in front of the cameras. The alignment of the laser sheets and cameras is shown in Fig. 2. The horizontally polarized laser sheet is aligned at the center of the sinusoidal riblet, while the vertically polarized laser sheet is located 0.5mm away in the spanwise direction from the horizontally polarized laser sheet.

Oil particles of normal $1 - 2$ μm diameter are produced with an array of Laskin nozzles and introduced passively upstream from the developing section. All cameras are adjusted in backward scatter configuration satisfying the Scheimpflug condition. The angle between the lens axis and the spanwise axis (orthogonal direction of measured planes) is set to be 30 degrees. The

scattering particle images in a size of 26×20 mm^2 are captured by high-speed CCD cameras (1284×1024 pixel^2) with 45μs pulse separation. The velocity vectors are yielded by spatial cross correlation of seeding images with a size of 32×8 pixel^2 (0.72×0.18 mm^2) interrogation window. An overlap of 50% is applied and high-frequency noise is filtered by a Gaussian filter with 3×3 kernel. The overlap is not applied for the calculation of the velocity gradients. The grid size is $\Delta x^+ = 5.4$ and $\Delta y^+ = 1.4$ in the case with the overlap and that is $\Delta x^+ = 10.8$ and $\Delta y^+ = 2.8$ in the case without the overlap. This grid size is very small and is comparable with that of the DNS. Since all instantaneous velocity vector fields of 2500 frames at 1000 fps are completely acquired on each plane, all nine velocity gradients can be calculated by using a second order central difference scheme on both in-plane and out-of-plane directions.

In order to validate the present DPS-PIV measurement system, statistics are compared with those performed by the 2D-PIV measurement [22]. Note that the present DPS-PIV system measures three velocity components, whereas the 2D-PIV system measures two velocity components. Hereafter, u, v, and w are velocities in the streamwise, wall-normal, and spanwise directions, respectively. All statistics are nondimensionalized by a friction velocity u_τ and viscosity ν. We use the friction velocity u_τ of the flow over the flat surface at a friction Reynolds number of 150. The procedure to estimate u_τ from the velocity field obtained by the present PIV measurement is as follows. The bulk mean velocity U_b is calculated by the integration of the streamwise velocity from location of the maximum streamwise velocity ($\delta_{u_{\max}}$) to the upper wall (i.e., flat wall side),

$$U_b = \frac{1}{l_x \left(2\delta - \delta_{u_{\max}}\right) T} \int_{\delta_{u_{\max}}}^{2\delta} \int_0^{l_x} \int_0^T u(x,y,t) dt dx dy, \tag{2}$$

where l_x is the measurement width in the streamwise direction, T is measurement time, and δ is the channel half height. The skin-friction coefficient C_f is defined as

$$C_f = \frac{\tau_w}{\frac{1}{2}\rho U_b^2} = 2\frac{u_\tau^2}{U_b^2}, \tag{3}$$

where we use the definition of the friction velocity ($u_\tau = \sqrt{\tau_w/\rho}$). The wall shear

stress and the density of the fluid are denoted by τ_w and ρ, respectively. There is an empirical formula for the skin-friction coefficient performed by Dean [33] and it reads

$$C_f = 0.073\mathrm{Re}_b^{-0.25} \tag{4}$$

where the bulk Reynolds number is defined as

$$\mathrm{Re}_b = \frac{2\delta U_b}{\nu}. \tag{5}$$

The empirical formula as shown in Eq. (4) is only for the flat surface case and the Reynolds number Re_b is computed by using the bulk velocity U_b of the flat side in Eq. (2). The friction velocity u_τ is used only for non-dimensionalization of the statistics for both riblet and flat sides. We isolate u_τ according to Eq. (3) and Eq. (4), i.e.,

$$u_\tau = U_b\sqrt{\frac{1}{2}0.073\mathrm{Re}_b^{-0.25}}. \tag{6}$$

Sasamori *et al.* [22] performed an experimental study for the flow over the sinusoidal riblet surface in the same wind tunnel with the present study. They measured the pressure difference at 275δ downstream from the inlet of the test section (the pressure taps are located at 187.5δ and 362.5δ) and the flow rate by a laminar flow mater and showed the drag reduction rate for different Reynolds numbers. As a result, the maximum drag reduction rate of sinusoidal riblet is 11.7% at $\mathrm{Re}_b \approx 3400$ corresponds to $\mathrm{Re}_\tau \approx 120$. The Reynolds numbers Re_b and Re_τ are based on the bulk and friction velocities, respectively.

In the following, we briefly summarize the estimation of the drag reduction rate in accordance with Sasamori *et al.* [22]. The drag reduction rate R_D is defined as

$$R_D = \frac{\tau_{\mathrm{flat}} - \tau_{\mathrm{riblet}}}{\tau_{\mathrm{flat}}}. \tag{7}$$

Here, τ_{flat} is the wall shear stresses where both the channel walls are the flat surface and it balances with the mean pressure gradient, as

$$\tau_{\mathrm{flat}} = -\delta_{\mathrm{flat}}(\frac{dp}{dx})_{\mathrm{flat}}. \tag{8}$$

In the present case, the upper and lower walls are the flat and the riblet surfaces respectively and the shear balance is

$$\tau'_{\rm flat} + \tau_{\rm riblet} = -2\delta_{\rm riblet}(\frac{dp}{dx})_{\rm riblet}. \tag{9}$$

This equation (9) is based on the symmetry of the channel flow between the walls. However, the flow statistics on the flat surface side agrees with the DNS data of the flat channel flow as shown in later. It implies that the influence of the riblet surface on the upper half of the channel lower wall (i.e., the flat surface side) is very small and $\tau_{\rm flat}$ in Eq. (8) is regarded to equal to $\tau'_{\rm flat}$ in Eq. (9). Therefore, the drag reduction rate R_D becomes,

$$R_D = 2\frac{\delta_{\rm flat}(\frac{dp}{dx})_{\rm flat} - \delta_{\rm riblet}(\frac{dp}{dx})_{\rm riblet}}{\delta_{\rm flat}(\frac{dp}{dx})_{\rm flat}}, \tag{10}$$

where the factor "2" arises. In order to consider the mass flow rate and the temperature, we use the total drag coefficient C_T instead of the mean pressure gradient. The definition of C_T is

$$C_T = \frac{8L_z^2\delta^3}{\frac{1}{2}\overline{\rho}\overline{Q}^2}\frac{{\rm d}p}{l}, \tag{11}$$

where L_z the channel span width, δ is the channel half height, ρ is the density, $\overline{Q}$ is the time averaged mass flow rate, $\overline{\rho}$ is the time averaged density, dp is the differential pressure, l is the distance between pressure tap. Thus, the drag reduction rate of Eq. (7) becomes

$$R_D = 2\frac{C_{T,\rm flat} - C_{T,\rm riblet}}{C_{T,\rm flat}}. \tag{12}$$

Since the uncertainty $U_{\rm RSS}$ (ANSI/ASME) [34] (95 % coverage) of R_D was approximately 16.8 % at ${\rm Re}_b \approx 3400$, they showed that R_D of the sinusoidal riblet is $9.8\% < R_D < 13.6\%$.

In the case of the optimal 2D riblet, the maximum drag reduction of 8% is obtained. For smaller h^+ or larger s_z^+, the drag reduction rate decreases or the drag increases. In contrast, the sinusoidal riblet surface reduces the drag at $h^+ = 6.3$ and $s_z^+ = 12$ to 60, i.e., the height is smaller and the lateral spacing is larger than those of the optimal 2D riblet.

In the present study of DPS-PIV measurement, the friction Reynolds number is also set to be $\mathrm{Re}_\tau = 150$, since Sasamori *et al.* [22] also performed PIV measurement at the same Reynolds number in which the drag reduction rate was approximately 10%.

2.2. Direct numerical simulation

In order to validate measurement results, we conduct a DNS of a fully developed channel flow with flat walls. The DNS code is based on that performed by Fukagata *et al.* [35]: for the time integration, the low storage third order Runge-Kutta method is used for advection terms and pressure terms and the Crank-Nicolson method is used for diffusion terms; for pressure-velocity coupling, the Simplified Marker and Cell (SMAC) method is used; for discretization of advection and diffusion terms, the energy conservative second order finite difference method and the second order central difference method are used, respectively. The computational domain is $(L_x \times L_y \times L_z) = (7.2 \times 2 \times 3.84)$ and the corresponding number of grids is $(N_x \times N_y \times N_z) = (512 \times 256 \times 2014)$. Periodic boundary conditions are applied in the homogeneous direction. The flow is incompressible and the governing equations are the continuity and Navier-Stokes equations. We imposed the constant mass flow rate condition and the bulk Reynolds number is set to $\mathrm{Re}_b = 4500$ (the corresponding skin-friction Reynolds number is $\mathrm{Re}_\tau \approx 150$). All variables are normalized by the twice bulk velocity $2U_b$ and the channel half height. The simulation starts from a fully developed flow.

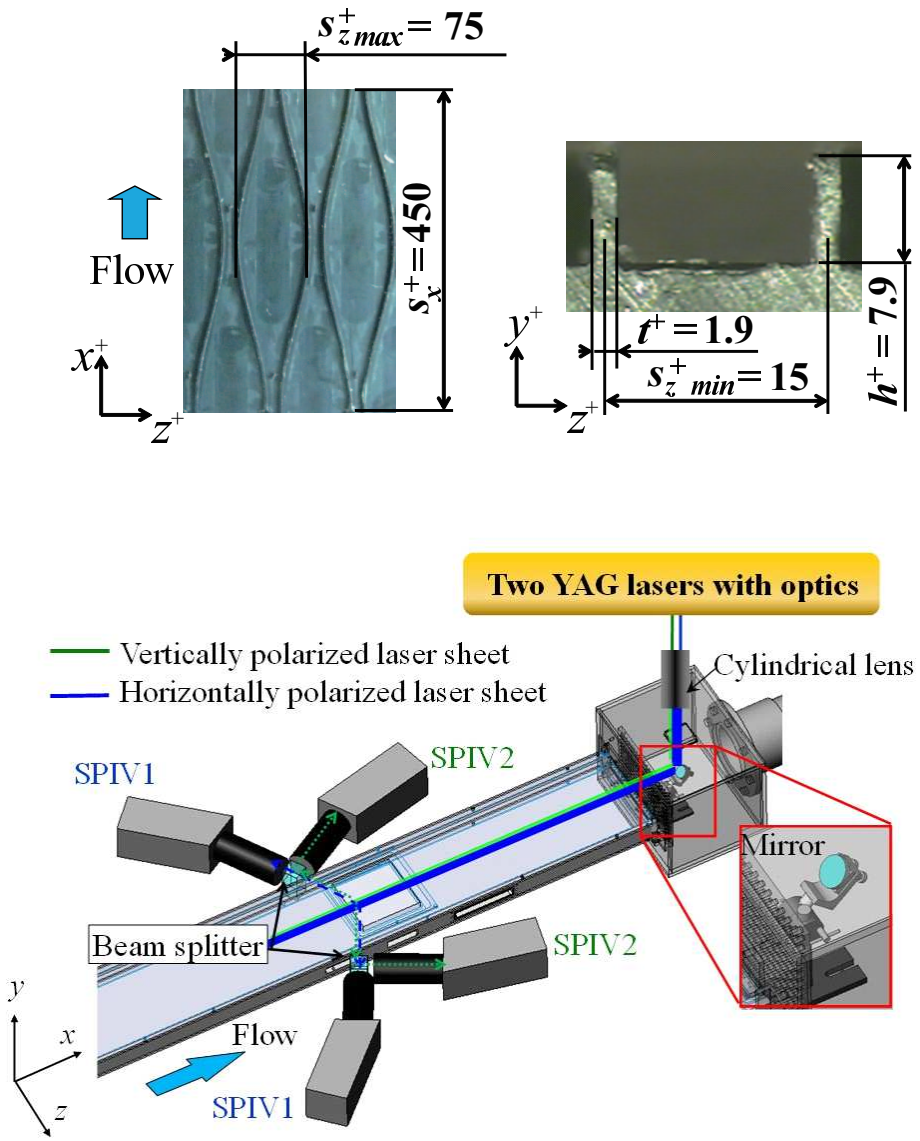

Figure 2: Schematic of dual-plane stereoscopic PIV system.

3. Result and discussion

3.1. Statistics

Figure 3 shows statistics at different measurement planes. The origin of the wall-normal coordinate is set to the surface of the bottom wall for the riblet and flat sides. In this figure, "$z^+ = 0$" indicates the measurement plane located at the center of the lateral spacing of the riblet walls and "$z^+ = 7.5$" indicates the measurement plane apart from the center plane. The statistics are nondimensionalized by the friction velocity of the flat side. The instantaneous velocity u_i is decomposed into a temporally averaged component $\langle u_i \rangle$ and a random component, u_i', as

$$u_i(x, y, t) = \langle u_i \rangle (x, y) + u_i'(x, y, t). \tag{13}$$

The rms values are obtained from $u_i'(x, y, t)$. In the flat side, reasonable agreement is obtained among the present DPS-PIV measurement, 2D-PIV measurement, and the DNS data. The obtained statistics reasonably agree with the DNS results for both measurement planes except the rms value of spanwise velocity. As discuss later, this error of the spanwise component influences on the profile of the streamwise vorticity. A similar trend is confirmed for other statistics as shown in Fig. 3(b)-(d). In the riblet side, the statistics at both measurement planes are smaller than those of the flat surface side and the difference between the measurement planes is small. We found that $\overline{u}$ by the DPS-PIV measurement also agrees with that by the 2D-PIV measurement: $\overline{u}$ in the buffer layer is smaller that of the flat surface side; $\overline{u}$ slightly is larger in the log layer. A similar tendency has been confirmed in the case of the v-groove riblet for the turbulent boundary layer flow [2] and the turbulent channel flow [5]. The rms values of velocities are shown in Fig. 4(b)-(d) and these values in the riblet case are smaller than that of the flat side.

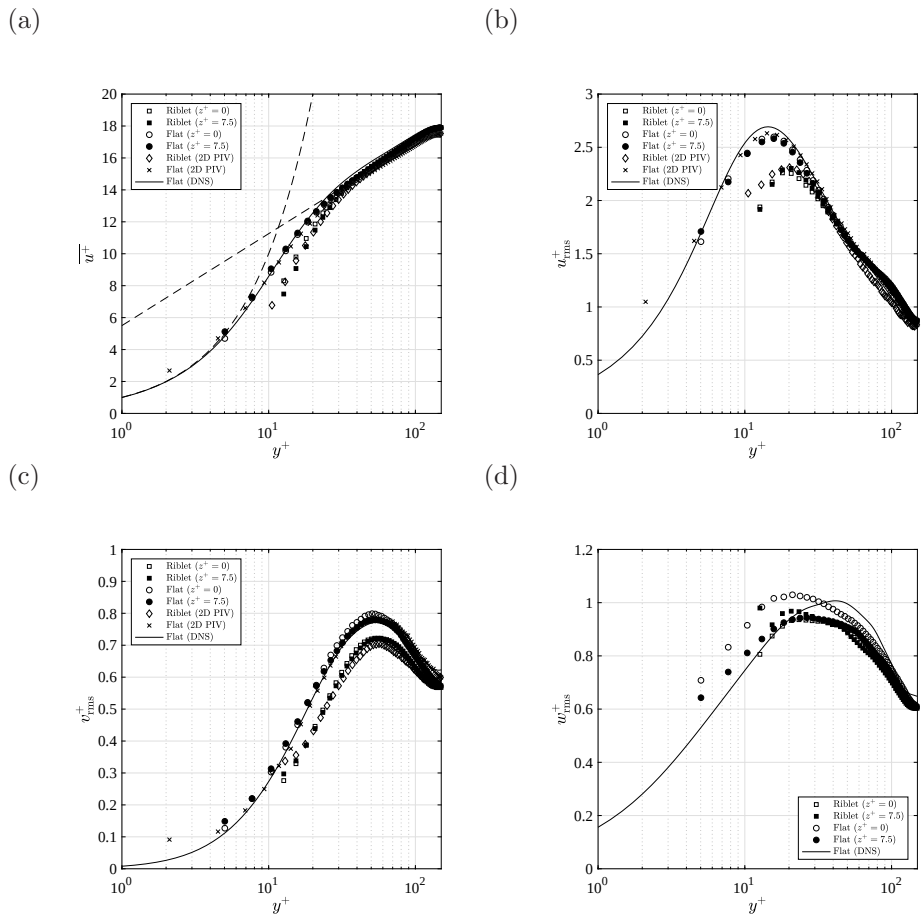

Figure 3: Mean profiles of (a) streamwise velocity, (b) u_{rms}, (c) v_{rms}, (d) w_{rms}, and (e) the RSS. The statistics are nondimensionalized by the friction velocity of the flat side.

Subsequently, we average the statistics of both measurement planes and show them in Fig. 4. Here, the statistics of the riblet side are nondimensionalized by the friction velocity of the riblet side considering the virtual origin. Procedure to compute them is as follows. First, we interpolate the profiles of the rms value of the streamwise velocity of the riblet and flat sides by a spline method. And we determine the friction velocity of the riblet side so that the peak value of the riblet side agrees that of the flat side. Second, we calculate the wall-shift y_0^+ of the riblet side by using the following equation [12], as

$$y_0^+ = \sqrt{\frac{2}{c_{f\,\mathrm{riblet}}}} - \sqrt{\frac{2}{c_{f\,\mathrm{flat}}}}, \tag{14}$$

where $c_{f\,\mathrm{riblet}}$ is computed by the obtained friction velocity of the riblet side. Figure 4(a) shows the mean streamwise velocity $\overline{u}$. In the flat case, reasonable agreement is obtained between the present DPS-PIV measurement and the DNS data. In the riblet case, good agreement is obtained in the buffer-layer and the velocity sift in the log-layer is observed. While good agreement of the rms value of the streamwise velocity is obtained as shown in Fig. 4(b), the difference appears in other statistics as shown in Fig. 4(c)-(e).

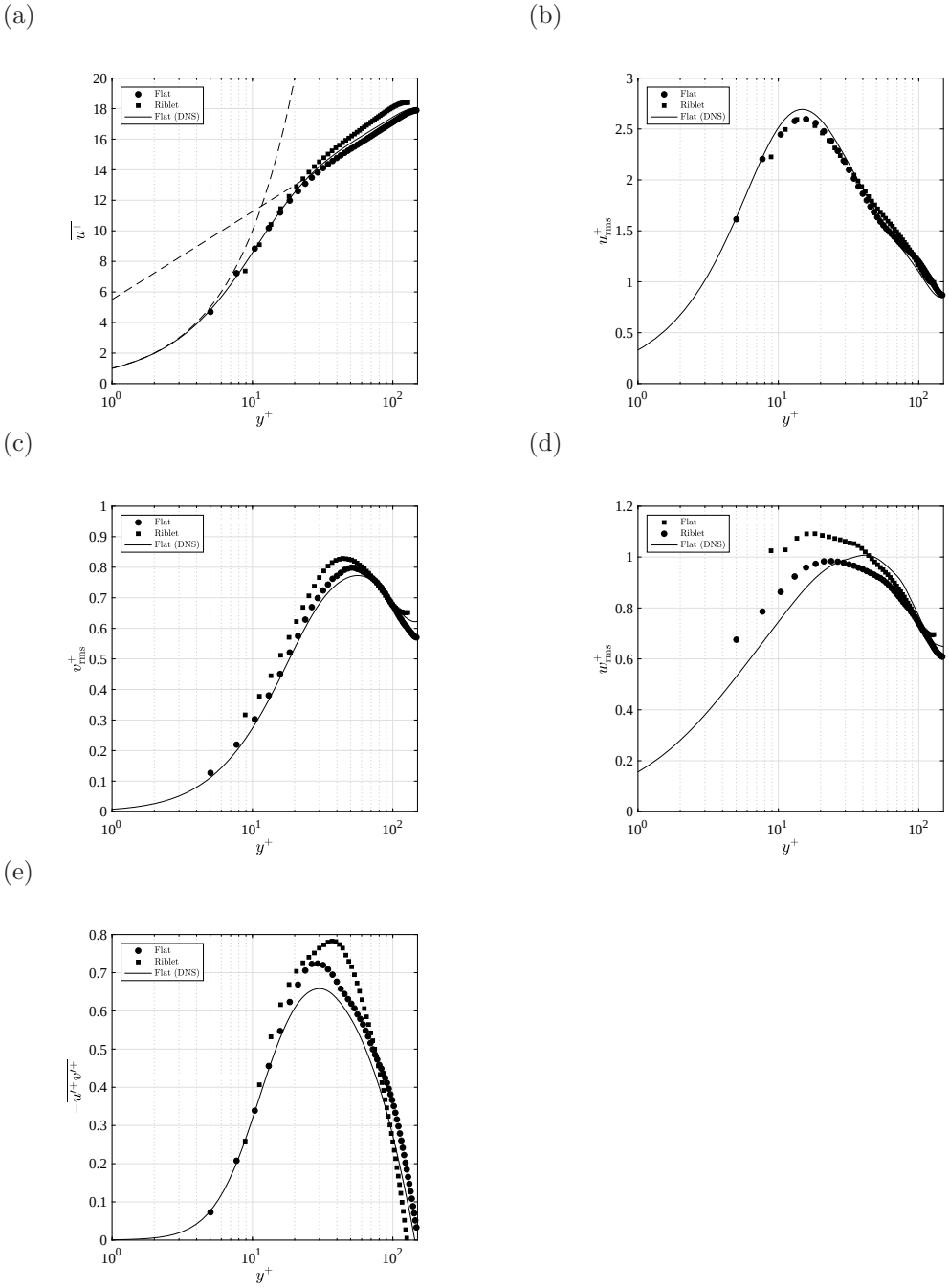

Figure 4: Mean profiles of (a) streamwise velocity, (b) u_{rms}, (c) v_{rms}, (d) w_{rms}, and (e) the RSS. The measurement plane located at the center of the lateral spacing of the riblet wall. The statistics of the riblet side are nondimensionalized by the friction velocity of the riblet side considering the virtual origin.

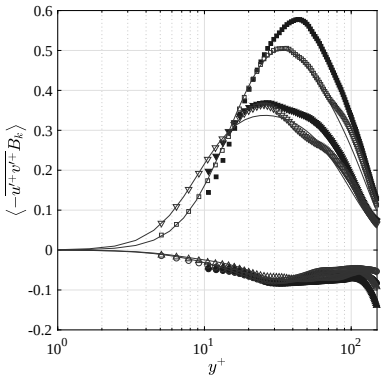

Figure 5: Reynolds shear stress from each quadrant in the case of the riblet. ∘, first quadrant; □, second quadrant; △, third quadrant; ▽, fourth quadrant. Filled and non-filled markers correspond to riblet and flat cases, respectively. Line are the DNS results.

We make the quadrant analysis for the RSS. The RSS is divided into four quadrants: the first quadrant ($u' > 0$, $v' > 0$) includes an outward interaction; the second quadrant ($u' < 0$, $v' > 0$) includes an ejection motion; the third quadrant ($u' < 0$, $v' < 0$) includes an inward interaction; the fourth quadrant ($u' > 0$, $v' < 0$) includes a sweep motion. The second and fourth quadrants are known to correspond to the activity of the quasi-streamwise vortex and contribute to increasing the RSS. Figure 5 shows profiles of each component of the RSS. The RSS is divided as

$$-\overline{u'^+v'^+} = \sum_{k=1}^{4} -\overline{u'^+v'^+}B_k. \tag{15}$$

Where B_k is the probability of each component. In the case of a flat surface, all quadrants reasonably agree the DNS data. The second and fourth quadrants dominate, whereas the first and third quadrant are small.

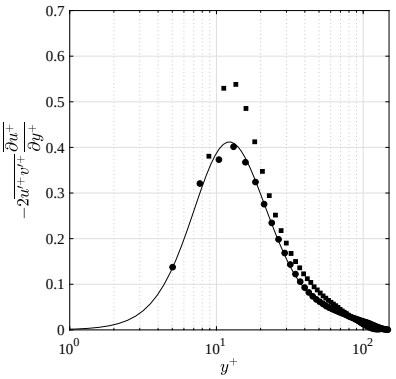

Figure 6: Production term of $\overline{u'^+u'^+}$: •, flat case by DPS-PIV; ■, riblet case by DPS-PIV; black line, the DNS results.

Figure 6 shows the profiles of the production term. In the flat side, there is reasonable agreement between the present result and the DNS result and we confirmed that it peaks at $y^+ \approx 13$. In the riblet side, the maximum value also locates at $y^+ \approx 13$ where the virtual origin is $y_0^+ \approx 2.2$. Since the riblet height is $h^+ = 7.5$ and the location of the riblet tip is $y_{tip}^+ = h^+ - y_0^+ = 5.3$, the riblet surface is immersed in the viscous sublayer. In the 2D case by Choi *et al.* [5], the drag decreases in the cases of which y_{tip}^+ is smaller than the viscous sublayer thickness ($y_{tip}^+ = 3.8$ and 6.6). In contrast with Choi *et al.* [5], we consider the 3D riblet surface, but y_{tip}^+ is also smaller than the viscous sublayer thickness.

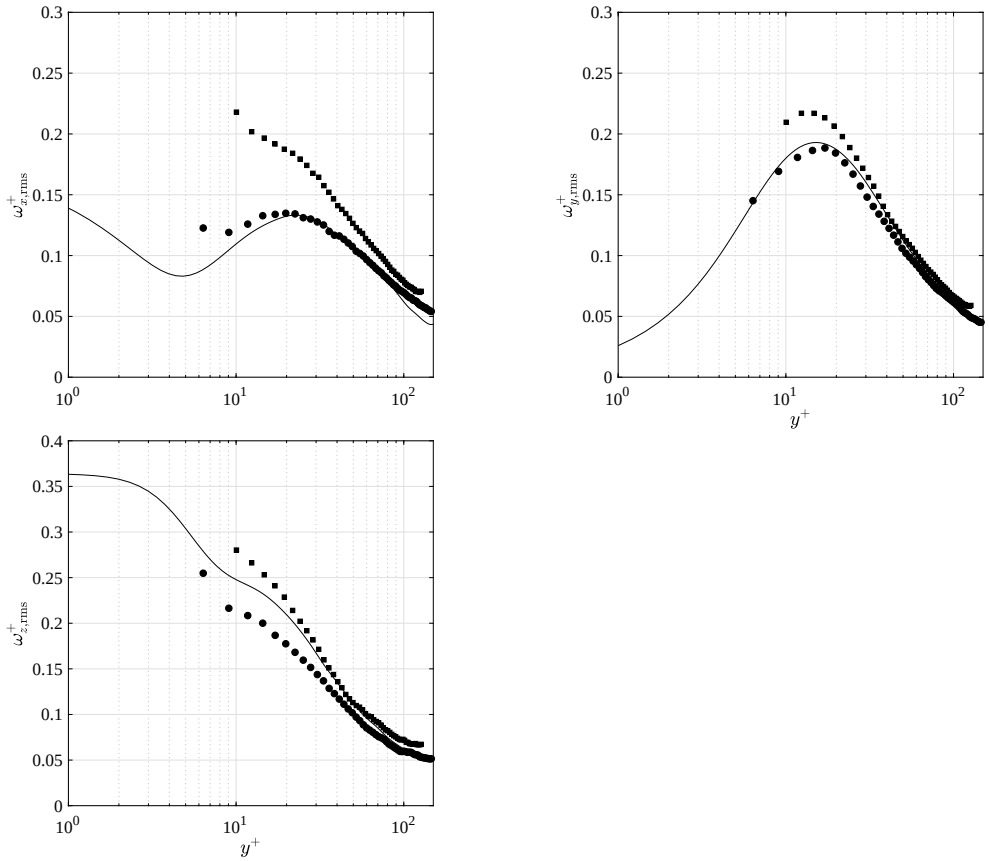

Figure 7: Profiles of the rms value of vorticity (a) $\omega^+_{x,\mathrm{rms}}$, (b) $\omega^+_{y,\mathrm{rms}}$, and (c) $\omega^+_{z,\mathrm{rms}}$. The measurement plane located at the center of the lateral spacing of the riblet wall: •, flat case by DPS-PIV; ■, riblet case by DPS-PIV; black line, the DNS results.

Figure 7 shows profiles of the rms value of vorticity, together with the DNS results. The vorticity consists of the velocity gradients which are computed without using the 50 % overlap. The reasonable agreement between the flat side and the DNS results is obtained, while the discrepancy appears since the velocity gradients more sensitive than other statistics. The increment of the streamwise vorticity is due to the measurement accuracy of the spanwise velocity component.

Figure 8 compares statistics in the flat surface case for different frame rates (1000 fps and 4000 fps) together the DNS results. The frame rate of 4000 fps is used at discussion of Q value as follows. The statistics at the center of the two laser sheets are shown. The reasonable agreement between different frame rate cases is obtained, while the rms value of the wall-normal vorticity in the 4000 fps case is overestimated as compared to the 500 fps case and the DNS results.

In the wall turbulence, the quasi-streamwise vortical structures exchange momentum between the regions near the wall and away from the wall. The quasi-streamwise vortical structures are often identified by using the second invariant of the velocity deformation tensor, called by the Q value (e.g., Kasagi *et al.* [25]). The Q value is defined as

$$Q = s'_{ij}s'_{ij} - \omega'_{ij}\omega'_{ij}, \tag{16}$$

where the symmetric part s'_{ij} and asymmetric part ω'_{ij} of deformation tensor are

$$s'_{ij} = \frac{1}{2}\left(\frac{\Delta u'_i}{\Delta x_j} + \frac{\Delta u'_j}{\Delta x_i}\right), \tag{17}$$

$$\omega'_{ij} = \frac{1}{2}\left(\frac{\Delta u'_i}{\Delta x_j} - \frac{\Delta u'_j}{\Delta x_i}\right), \tag{18}$$

respectively. Figure 9 shows a grid system for the measurement. The velocities are measured on the corner of the cell (denoted by the black circle). We interpolate velocities into the center between them (i.e., denoted by the black triangle) and calculate the velocity gradient at the center of the cell (denoted by the square). Since two laser sheets are provided, all the nine velocity gradients are obtained at the center of the two laser sheets. Thus the Q value can be obtained by using Eq. (16).

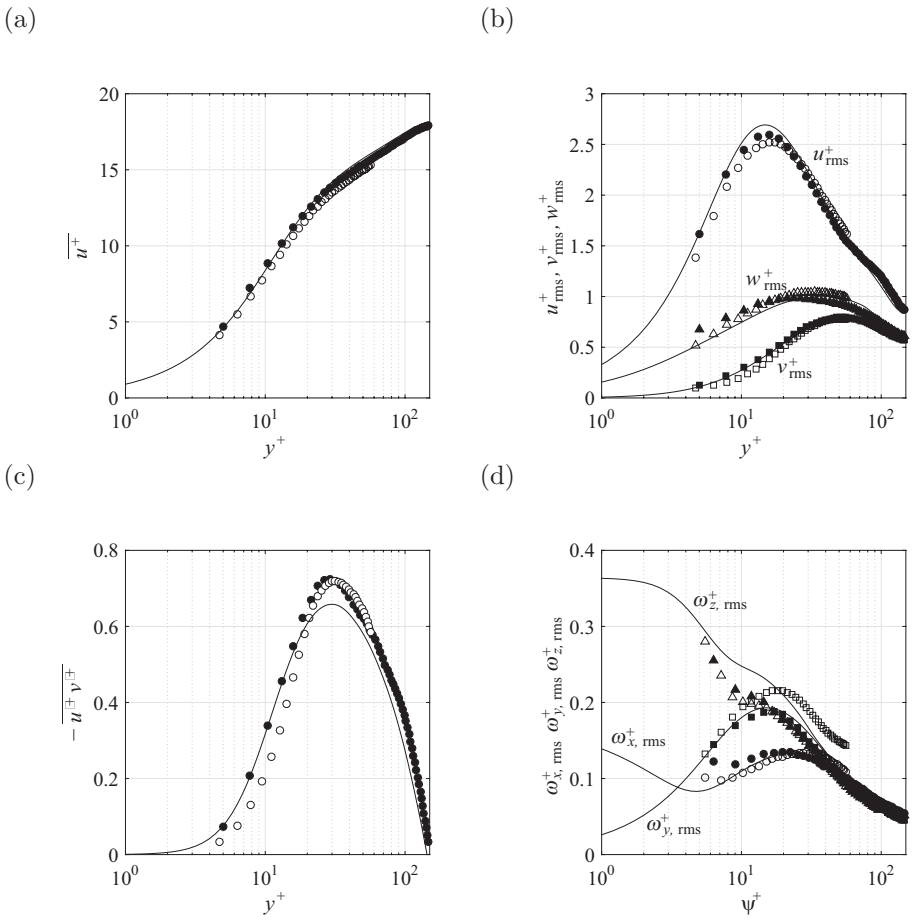

Figure 8: Mean profiles in flat case: (a) streamwise velocity; (b) RMS values of velocities; (c) RSS; (d) RMS values of vorticities. Filled symbol, 1000 fps; blank symbol, 4000 fps; black line, the DNS results.

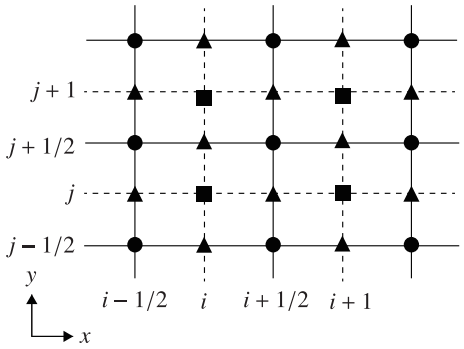

Figure 9: Grid for calculation of velocity gradient: circle, measured velocities; triangle, interpolated velocities; square, gradient of velocities.

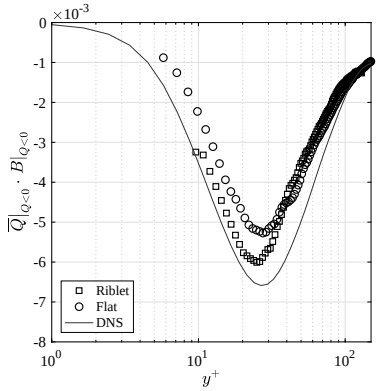

Figure 10: Profiles of negative Q^+ over the smooth and riblet surfaces.

(a) (b)

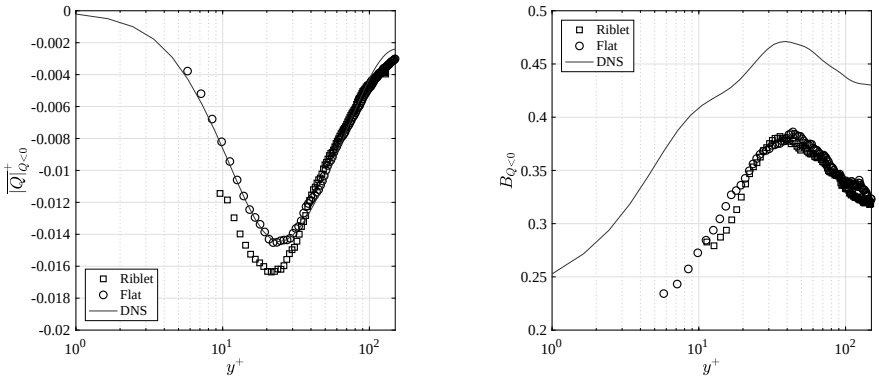

Figure 11: Profiles of intensity and probability of negative Q^+ over the smooth and riblet surfaces.

The $\overline{Q}$ value, averaged in time and streamwise direction, consists of positive and negative contributions, i.e.,

$$\overline{Q} = \overline{Q}\big|_{Q>0} \cdot B|_{Q>0} + \overline{Q}\big|_{Q<0} \cdot B|_{Q<0}\,. \tag{19}$$

The profile of $\overline{Q}\big|_{Q<0} \cdot B|_{Q<0}$ is shown in Fig. 10. As compared with the DNS results, the measured Q value of the flat surface case is underestimated. This is due to an underestimation of the probability B as shown in Fig. 11(b), whereas the intensity of the Q value in the flat side agrees with that by the DNS results as shown in Fig. 11(a). At $y^+ < 30$, the intensity and probability in the riblet

surface case are smaller than those of the flat case. On the other hand, at $y^+ > 30$, the probability almost agrees with that of the flat surface and it implies that the "structure" of vortical structure does not change due to the riblet.

3.2. Vortical structure

In the following subsections, we compare the behavior of the vortical structure between the riblet and flat sides. The vortical structures are displaced away from the wall, which is major mechanism of the drag reduction effect by the sinusoidal riblet and has been confirmed by the pathline analysis [22]. Instead of the pathline analysis, we directly measure and track the vortical structure by using Q value. To clarify the displacement of the vortical structure, the origin of the wall-normal coordinate is set to be the location of the lower wall surface and the friction velocity of the flat surface is used for both riblet and flat sides in the following. Therefore, the "channel half-width" corresponds the distance between the lower wall and the center of the channel. Sasamori *et al.* [22] compared the channel half-width and that determined from the cross-sectional area and the wetted perimeter. Since the difference between them was $8.8 \times 10^{-2}\%$, they used the distance between the channel walls as the channel half-width. The present paper therefore is in accordance with it.

Figures 12 and 13 show instantaneous flow fields over the flat and riblet surfaces, respectively. The horizontal and vertical axes are the streamwise and wall-normal coordinates, respectively. The direction of the base flow is from left to right. The lateral spacing of the riblet is at a maximum at $x^+ \approx 180$, expands in the region of $0 < x^+ < 180$ and contracts in the region of $180 < x^+ < 360$. The color contour shows the distribution of the Reynolds shear stress (strictly speaking, the product of instantaneous velocity fluctuations) and spanwise velocity fluctuation. The black line is an isoline of $Q^+ = -0.01$. Here, spatial resolutions in both flat and riblet cases are $\Delta x^+ = 10.8$, $\Delta y^+ = 2.8$ and $\Delta z^+ = 7.6$. As shown in Figs. 12 and 13, the present DPS-PIV measurement captures vortical structures: the region enclosed by the isoline of $Q^+ = -0.01$ is inclined in the streamwise direction and the positive RSS and w' are found around them. However, no major difference is observed between the flat and riblet cases.

Negative Q^+ is appropriate to detect the vortical structures, and a conditional averaging is conducted below. We searched for a local minimum of the

Q value on a line of $y^+ = 30$ (parallel to the horizontal axis), extracted the flow field around the local minimum, and averaged the flow field in time. Figure 14(a) shows the conditionally averaged vortical structure in the flat case. The inclination angle and diameter of the vortical structure are approximately 10 degree and 30 in the wall unit, respectively. The inclination angle θ_{xy} is computed by

$$\theta_{xy} = \arctan\left(\frac{\omega_y'^+}{\omega_x'^+}\right). \tag{20}$$

We obtained 10 degree at the core of the vortical structure. The inclined angle is slightly larger than the shear-layer front angle of 5 degrees [36] and it of 8 degrees [37] based on space-time correlation. The minimum Q^+ value is -0.034 and the induced spanwise velocity fluctuation is observed. Figure 14(b) shows the riblet case. The spanwise velocity fluctuation is found to decrease as compared with that of the flat case. The minimum Q^+ value is -0.031 which shows a slight recovery from that of the flat case.

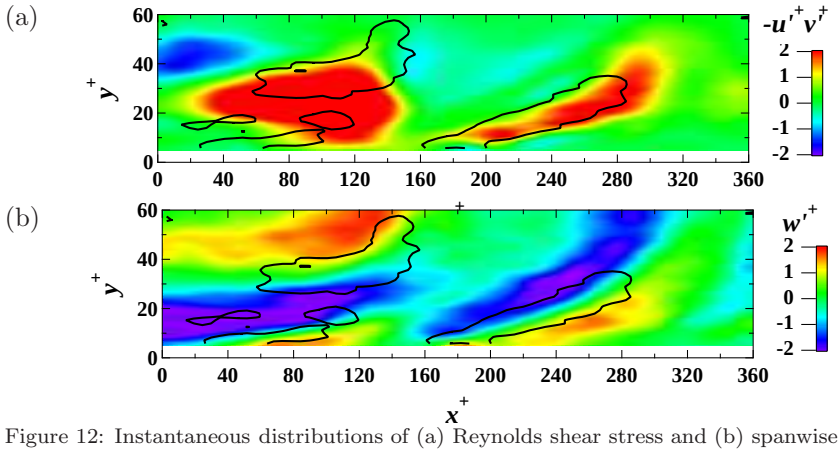

Figure 12: Instantaneous distributions of (a) Reynolds shear stress and (b) spanwise velocity fluctuation for a smooth surface. Black line is the isoline of $Q^+ = -0.01$.

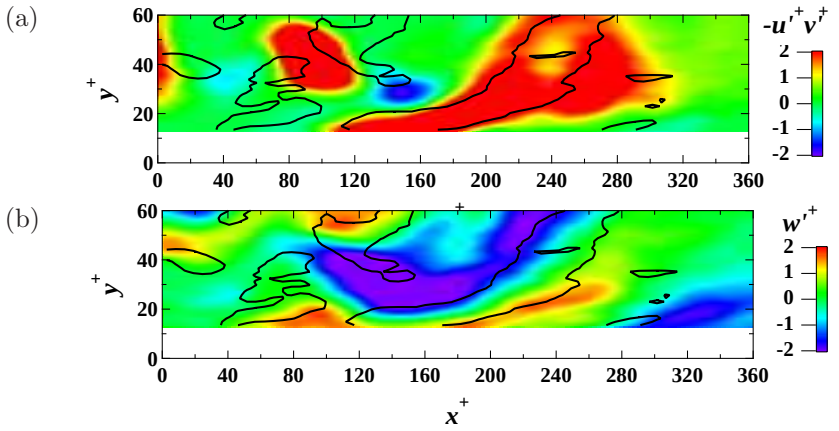

Figure 13: Instantaneous distributions of (a) Reynolds shear stress and (b) spanwise velocity fluctuation for the riblet surface. The black line is the isoline of $Q^+ = -0.01$.

(a)

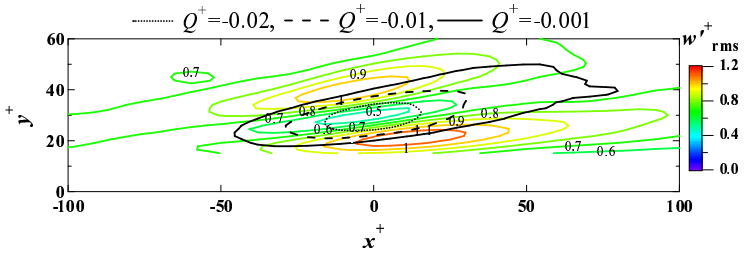

(b)

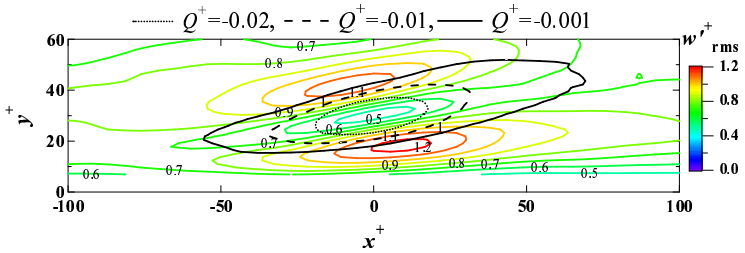

Figure 14: Conditional sampled Q^+ and w^+_{rms} of (a) the smooth and (b) the sinusoidal riblet surfaces.

3.3. Tracking of vortical structure

In this section, as an extension of Sasamori *et al.*'s [22] pathline analysis, we directly track the vortical structure by using a measured Q value in order to observe the behavior of the vortical structure over the riblet. The frame rate of PIV measurement is changed from 1000 to 4000 fps to track the vortical structure accurately. The corresponding time interval becomes $\Delta t^+ = 1.8$. The procedure of vortex tracking is explained in Fig. 15 and as follows;

- set the threshold value of $Q^+ = -0.01$ and count the region of $Q^+ \leq -0.01$ as "the vortical structure";
- calculate the weighted center-of-gravity of the vortical structure and named it "the core";
- predict the core position in the next time step (named as "predicted core") using the local velocity at the present core position;
- define the "search area" centering the predicted core and width and height of the search area are $u^+_{\mathrm{rms}}(x,y) \times \Delta t^+$ and $v^+_{\mathrm{rms}}(x,y) \times \Delta t^+$, respectively;
- use the flow field in the next time step image (i.e., $t^+ = t^+_0 + \Delta t^+$) and calculate the core position;
- calculate the advection distance of the vortical structure if the core exists in a search region.

Figure 16 shows a sample of the vortex tracking. Some cores are detected (named "A" to "G") and their trajectories are calculated. The vortical structures of "A" to "E" are observed from $t^+ = t^+_0$ to $t^+ = t^+_0 + \Delta t^+$, whereas "F" disappears and "G" appears, respectively. Note that the displacement is evaluated for "A" to "E" but not for "F" and "G".

In order to evaluate the displacement of the vortical structure quantitatively, we calculate the probability of the wall-normal displacement of the vortical structure. We make a grid as shown in Fig. 17: the lower cells are located at $11 < y^+ < 25$ and the upper cells are located at $25 < y^+ < 60$; the width of the

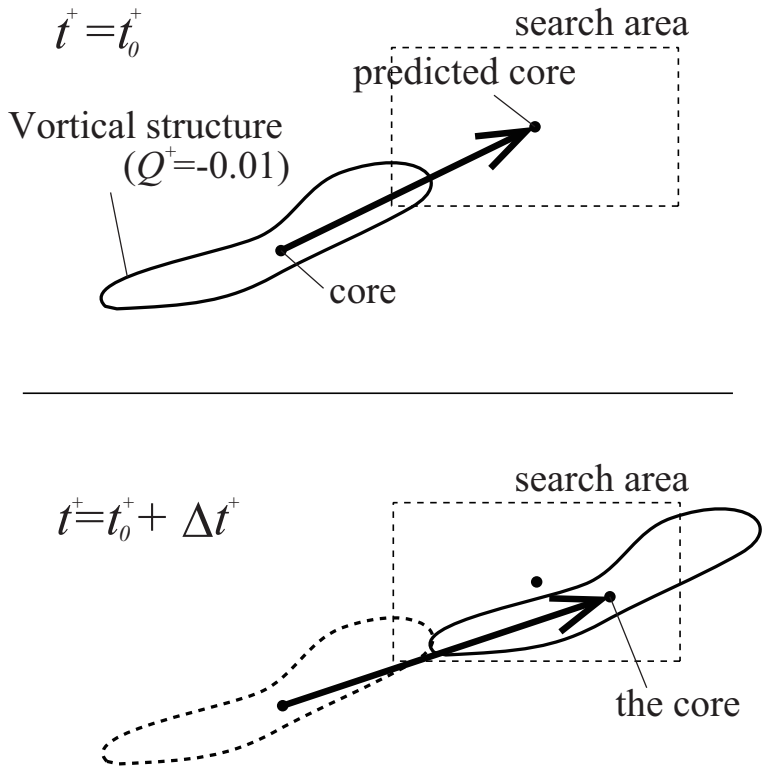

Figure 15: Schematic of vortex tracking.

cell is 40 in the wall unit; 18 sections are provided. If the vortical structure, for example, shifts upward (or the displacement of the center-of-gravity is positive), we count it as a positive displacement, i.e., $I_{up,i} = 1$ and $I_{down,i} = 0$. If the vortical structure moves toward the wall, we count $I_{up,i} = 0$ and $I_{down,i} = 1$. Here I is the counter and is defined at each cell. This process is followed for all velocity fields. The subscript of i denotes the order of the velocity field. The probability function of wall-normal displacement of the vortical structure

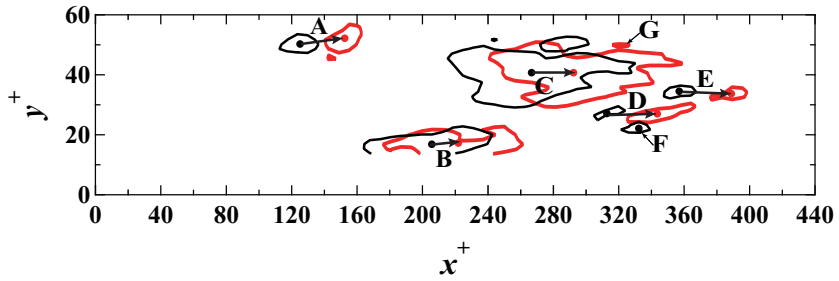

Figure 16: Instantaneous distribution of Q^+ and its core. The black and red lines are the isolines of $Q^+ = -0.01$ at (a) $t^+ = t_0^+$ and (b) $t^+ = t_0^+ + \Delta t^+$. The solid circle marker represents the core of the vortical structure. The arrow indicates the trajectories of each vortical structure.

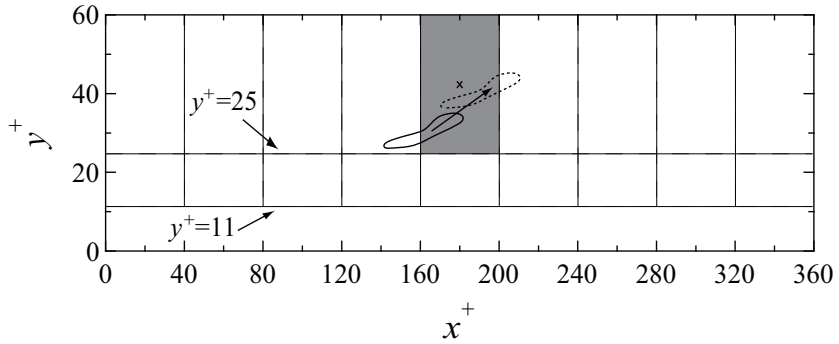

Figure 17: The mesh for the probability calculation.

is defined as

$$P_{up} = \frac{\sum_i I_{up,i}}{\sum(I_{down,i} + I_{up,i})}, \tag{21}$$

$$P_{down} = \frac{\sum_i I_{down,i}}{\sum(I_{down,i} + I_{up,i})}. \tag{22}$$

Here, P_{up} and P_{down} denote the probability of the vortical structure leaving the wall and moving toward the wall, respectively. Note that the sum of P_{up} and P_{down} equals one.

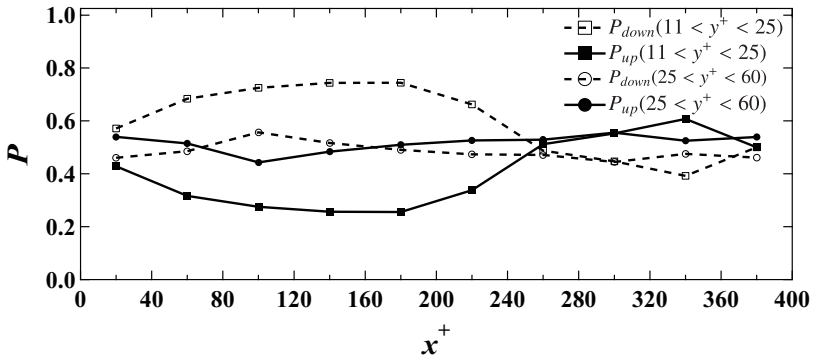

Figure 18: Probability density function of the sign of vortex displacement in the wall-normal direction in the riblet surface case.

Figure 18 shows the probability. In the range of $20 < x^+ < 250$, P_{down} of the lower cell increases whereas P_{up} of the lower cell decreases. This indicates that the vortical structure, traveling in the region near the wall, approaches the wall where the lateral spacing of the riblet walls is expanding. At $250 < x^+ < 330$, $P_{up}(11 < y^+ < 25)$ is over 0.5, indicating that the vortical structure leaves the wall region. On the other hand, P_{down} and P_{up} of $25 < y^+ < 60$ are 0.5 approximately, which implies the vortical structure travels in the streamwise direction without approaching or leaving the wall.

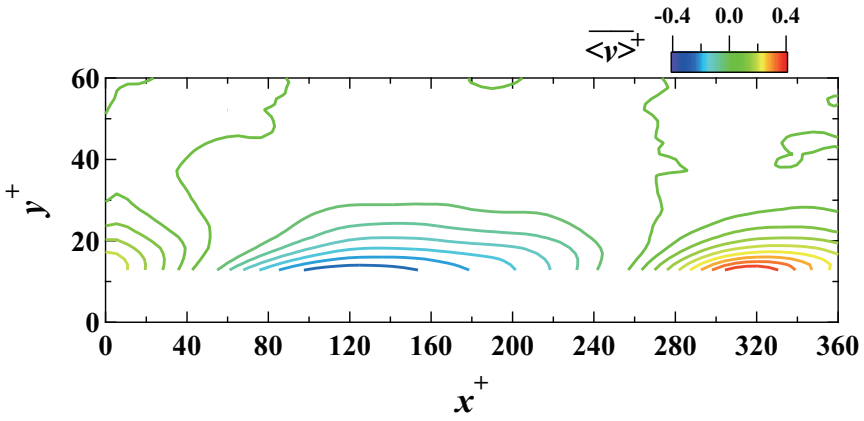

Figure 19: Distribution of time-averaged wall-normal velocity over the riblet surface.

Figure 19 shows the distribution of the time-averaged wall-normal velocity. In the region near the wall, the wall-normal velocity is negative at $20 < x^+ < 260$ whereas it is positive at $0 < x^+ < 20$ and $260 < x^+ < 360$. The upward and downward flows are induced by the sinusoidal riblet surface. The probability of the vortical structure leaving the wall increases where the upward flow is induced, whereas the probability of the vortical structure approaching the wall increases where the downward flow is induced. Even if the vortical structure in the region near the wall moves toward the wall, it leaves the near wall region due to the upward flow induced by the sinusoidal riblet surface.

In the sinusoidal riblet case, the vortical structures are displaced away from the wall and it results in the skin-friction drag reduction. According to theoretical and numerical analyses by Iwamoto *et al.* [38], the turbulence in the outer layer decreases if the near wall turbulence is damped under the constant flow rate condition in the channel flow. This effect is confirmed in the boundary layer flow [39]. This mechanism is similar to the that in the 2-D riblets, although the lateral spacing of the sinusoidal riblet is larger than those of the 2-D riblet and the diameter of streamwise vortices.

4. Conclusion

Dual-plane stereoscopic PIV measurement for the turbulent channel flow over the smooth and sinusoidal riblet surfaces was performed. The sinusoidal riblet surface provided 11.7% of the drag reduction as compared with that of the flat surface. The advantage of the sinusoidal riblet surface is that it has large lateral spacing of the adjacent walls of the riblet surface as compared with that of the 2D riblet. The PIV measurement was carried out in a channel flow at the friction Reynolds number of 150. The obtained statistics show reasonable agreement with the previous studies. Since the present PIV measurement system provides all the nine velocity gradients, the second invariant of the deformation tensor Q^+ was calculated and quasi-streamwise vortical structures were identified. We found the probability Q^+ value over the riblet surface did not change at $y^+ > 30$, indicating that "structure" does not change.

In contrast to the previous pathline analysis, we directly measure the core of the vortical structure by using Q value and made the analysis of vortex tracking. The result shows that the vortical structure in the region near the wall follows the upward and downward flows induced by the sinusoidal riblet surface. Therefore, the drag reduction effect is obtained although the wetted area of the sinusoidal riblet is small. The obtained results support the discussion made by previous studies [22, 23]: the riblet prevents the vortex hitting the wall, which is similar in the case of the 2D riblet surface.

Acknowledgments

This research was partially supported by the Ministry of Education, Culture, Sports, Science and Technology through a Grant-in-Aid for Scientific Research (c) of 15K05785 in 2015. The sinusoidal riblet plates in this research were fabricated by using a milling machine at Tokyo University of Agriculture and Technology Center of Design and Manufacturing.

References

[1] M. J. Walsh, Drag characteristics of v-groove and transverse curvature riblets, Symp. Viscous Flow Drag Reduct 72 (1980) 169–184.

[2] M. J. Walsh, Turbulent boundary layer drag reduction using riblets, Am. Inst. Aeronaut. Astronaut. 9 (1982) AIAA–paper 82–0169.

[3] M. J. Walsh, Riblets as a viscous drag reduction technique, Am. Inst. Aeronaut. Astronaut. 21 (1983) 485–486.

[4] D. Bechert, M. Bruse, W. Hage, J. T. Van der Hoeven, G. Hoppe, Experiments on drag-reducing surfaces and their optimization with an adjustable geometry, J. Fluid Mech. 338 (1997) 59–87.

[5] H. Choi, P. Moin, J. Kim, Direct numerical simulation of turbulent flow over riblets, J. Fluid Mech. 255 (1993) 503–539.

[6] O. El-Samni, H. Chun, H. Yoon, Drag reduction of turbulent flow over thin rectangular riblets, Int. J. Engineer. Sci. 45 (2007) 436–454.

[7] R. García-Mayoral, J. Jiménez, Scaling of turbulent structures in riblet channels up to $\mathrm{Re}_\tau \approx 550$, Phys. Fluids 24 (2012) 105101, 23 pp.

[8] A. Boomsma, F. Sotiropoulos, Riblet drag reduction in mild adverse pressure gradients: A numerical investigation, Int. J. Heat Fluid Flow 56 (2015) 251–260.

[9] S.-J. Lee, S.-H. Lee, Flow field analysis of a turbulent boundary layer over a riblet surface, Exp. Fluids 30 (2001) 153–166.

[10] Y. Suzuki, N. Kasagi, Turbulent drag reduction mechanism above a riblet surface, AIAA J 32 (1994) 1781–1790.

[11] D. Gatti, M. Quadrio, Reynolds-number dependence of turbulentskin-friction drag reduction induced byspanwise forcing, J. Fluid Mech. 802 (2016) 553–582.

[12] P. Spalart, J. D. McLean, Drag reduction: enticing turbulence, and then an industry., Phil. Trans. R. Soc. A 369 (2011) 1556–1569.

[13] P. Luchini, Reducing the turbulent skin friction, in: Computational methods in applied sciences '96, 1996.

[14] D. Bechert, M. Bartenwerfer, The viscous flow on surfaces with longitudinal ribs, J. Fluid Mech. 206 (1989) 105–129.

[15] P. Luchini, F. Manzo, A. Pozzi, Resistance of a grooved surface to parallel flow and cross-flow, J. Fluid Mech. 228 (1991) 87–109.

[16] D. W. Bechert, M. Bruse, W. Hage, Experiments with three-dimensional riblets as an idealized model of skark skin, Exp. Fluids 28 (2000) 403–412.

[17] Y. Peet, P. Sagaut, Y. Charron, Turbulent drag reduction using sinusoidal riblets with triangular cross-section, AIAA paper 3745 (2008).

[18] Y. Peet, P. Sagaut, Theoretical prediction of turbulent skin friction on geometrically complex surfaces, Phys. Fluids 21 (2009) 105105, 19 pp.

[19] K. Okabayashi, Direct numerical simulation for modification of sinusoidal riblets, J. Flud Sci. Thechnol. 11 (2016) 16–00355, 16 pp.

[20] K. Okabayashi, Direct numerical simulation for investigation on yaw angle effects on riblets, J. Flud Sci. Thechnol. 12 (2017) 16–00501, 11 pp.

[21] H. Benschop, W.-P. Breugem, Drag reduction by herringbone riblet texture in direct numerical simulations of turbulent channel flow, J. Turbulence 18 (2017) 43 pp.

[22] M. Sasamori, H. Mamori, K. Iwamoto, A. Murata, Experimental study on drag-reduction effect due to sinusoidal riblets in turbulent channel flow, Exp. Fluids 55 (2014) 1–14.

[23] M. Sasamori, O. Iihama, H. Mamori, K. Iwamoto, A. Murata, Parametric study on a sinusoidal riblet for drag reduction by direct numerical simulation, Flow Turbul. Combst. 99 (2017) 47–69.

[24] J. C. Hunt, A. Wray, P. Moin, Eddies, streams, and convergence zones in turbulent flows, Center for Turbulence Research Proc. the Summer Program 1988 (1988) 193–208.

[25] N. Kasagi, Y. Sumitani, Y. Suzuki, O. Iida, Kinematics of the quasi-coherent vortical structure in near-wall turbulence, Int. J. Heat Fluid Flow 16 (1995) 2–10.

[26] M. Tanahashi, S.-J. Kang, T. Miyamoto, S. Shiokawa, T. Miyauchi, Scaling law of fine scale eddies in turbulent channel flows up to $\mathrm{Re}_\tau = 800$, Int. J. Heat Fluid Flow 25 (2004) 331–340.

[27] C. Kähler, J. Kompenhans, Multiple plane stereo piv: Technical realization and fluid-mechanical significance, in: Proc. the 3rd International Workshop on PIV, 1999, pp. 16–18.

[28] H. Hu, T. Saga, T. Kobayashi, N. Taniguchi, M. Yasuki, Dual-plane stereoscopic particle image velocimetry: system set-up and its application on a lobed jet mixing flow, Exp. Fluids 31 (2001) 277–293.

[29] J. A. Mullin, W. J. A. Dahm, Dual-plane stereo particle image velocimetry measurements of velocity gradient tensor fields in turbulent shear flow. II. Experimental results, Phys. Fluids 18 (2006) 035102, 28 pp.

[30] J. A. Mullin, W. J. Dahm, Dual-plane stereo particle image velocimetry (DSPIV) for measuring velocity gradient fields at intermediate and small scales of turbulent flows, Exp. Fluids 38 (2005) 185–196.

[31] J. A. Mullin, W. J. Dahm, Dual-plane stereo particle image velocimetry measurements of velocity gradient tensor fields in turbulent shear flow. I. Accuracy assessments, Phys. Fluids 18 (2006) 035101, 18 pp.

[32] M. Tanahashi, T. Hirayama, S. Taka, T. Miyauchi, Measurement of fine scale structure in turbulence by time-resolved dual-plane stereoscopic PIV, Int. J. Heat Fluid Flow 29 (2008) 792–802.

[33] R. Dean, Reynolds number dependence of skin friction and other bulk flow variables in two-dimensional rectangular duct flow, J. Fluids Engineer. 100 (1978) 215–223.

[34] ANSI/ASME, Measurement uncertainty, supplement on instru-ments and apparatus (1987).

[35] K. Fukagata, N. Kasagi, P. Koumoutsakos, A theoretical prediction of friction drag reduction in turbulent flow by superhydrophobic surfaces, Phys. Fluids 18 (2006) 051703, 4 pp.

[36] H.-P. Kreplinp, H. Eckelmann, Propagation of perturbations in the viscous sublayer and adjacent wall region, J. Fluid Mech. 95 (1979) 305–322.

[37] H. Rebbeck, K.-S. Choi, A wind-tunnel experiment on real-time opposition control of turbulence, Phys. Fluids 18 (2006) 035103, 13 pp.

[38] K. Iwamoto, K. Fukagata, N. Kasagi, Y. Suzuki, Friction drag reduction achievable by near-wall turbulence manipulation at high Reynolds numbers, Phys. Fluids 17 (2005) 011702, 4 pp.

[39] A. Bannier, E. Garnier, P. Sagaut, Friction drag reduction achievable by near-wall turbulence manipulation in spatially developing boundary-layer, Phys. Fluids 28 (2016) 035108, 16 pp.